Dalton Transactions

ROYAL SOCIETY OF CHEMISTRY

PAPER

View Article Online
View Journal | View Issue

Cite this: *Dalton Trans.*, 2020, **49**, 15287

The first pentagonal-bipyramidal vanadium(III) complexes with a Schiff-base N_3O_2 pentadentate ligand: synthesis, structure and magnetic properties†

Tamara A. Bazhenova,*[a] Leokadiya V. Zorina,[b] Sergey V. Simonov,[b] Vladimir S. Mironov,*[a,c] Olga V. Maximova,[a,d,e] Lena Spillecke,*[f] Changhyun Koo,[f] Rüdiger Klingeler,[f,g] Yuriy V. Manakin,[a] Alexander N. Vasiliev[d,h] and Eduard B. Yagubskii*[a]

A series of three mononuclear pentagonal-bipyramidal V(III) complexes with the equatorial pentadentate N_3O_2 ligand (2,6-diacethylpyridinebis(benzoylhydrazone), H_2DAPBH) in the different charge states (H_2DAPBH^0, $HDAPBH^{1-}$, $DAPBH^{2-}$) and various apical ligands (Cl^-, CH_3OH, SCN^-) were synthesized and characterized structurally and magnetically: $[V(H_2DAPBH)Cl_2]Cl{\cdot}C_2H_5OH$ (**1**), $[V(HDAPBH)(NCS)_2]{\cdot}0.5CH_3CN{\cdot}0.5CH_3OH$ (**2**) and $[V(DAPBH)(CH_3OH)_2]Cl{\cdot}CH_3OH$ (**3**). All three complexes reveal paramagnetic behavior, resulting from isolated $S = 1$ spins with positive zero-field splitting energy expected for the high-spin ground state of the V^{3+} ($3d^2$) ion in a PBP coordination. Detailed high-field EPR measurements for compound **3** show that its magnetic properties are best described by using the spin Hamiltonian with the positive ZFS energy ($D = +4.1$ cm^{-1}) and pronounced dimer-like antiferromagnetic spin coupling ($J = -1.1$ cm^{-1}). Theoretical analysis based on superexchange calculations reveals that the long-range spin coupling between distant V^{3+} ions (8.65 Å) is mediated through π-stacking contacts between the planar $DAPBH^{2-}$ ligands of two neighboring $[V(DAPBH)(CH_3OH)_2]^+$ complexes.

Received 4th September 2020,
Accepted 5th October 2020

DOI: 10.1039/d0dt03092a

rsc.li/dalton

Introduction

In recent years, 3d and 4f complexes with the 2,6-diacetylpyridine-based acyclic ligands (see Fig. S1, ESI†) have attracted growing interest as advanced molecular magnetic materials.[1,2] In particular, some of these complexes are field-induced single-ion magnets (SIMs);[1] they are also used as anisotropic spin units in designing polynuclear single-molecule magnets (SMMs) and single-chain magnets (SCMs).[1a,2] The complexes of 3d metals with these ligands frequently adopt a pentagonal-bipyramidal (PBP, D_{5h}-symmetry) geometry around the central metal atom resulting from the pentagonal coordination (N_3O_2) of almost planar pentadentate ligands in the equatorial plane and two apical ligands (usually solvent molecules and/or Cl^-, NO_3^-, N_3^-, SCN^- anions).[3] These PBP complexes are attractive building blocks for assembling polynuclear magnetic structures, especially since their labile apical ligands can easily be substituted by various bridging units. It is also essential that, unlike the closed-ring macrocyclic ligands (of N_3O_2 and N_5 types),[4] the open acyclic ligands (N_3O_2) can occur in three charge states, neutral (protonated, A), monoanionic (monodeprotonated, C) and dianionic (dideprotonated, B), Fig. S1, ESI,† thereby extending the variety of metal complexes.

The interest in magnetic metal complexes with the 2,6-diacetylpyridine-based acyclic ligands is largely caused by their PBP geometry that in many cases produces the ground spin state with a significant magnetic anisotropy; the latter is currently recognized as the most critical factor in the development of high-performance SMMs.[5] Particularly, the PBP coordination provides a strong uniaxial magnetic anisotropy for metal ions with enhanced spin–orbit coupling (4d, 5d and 4f

[a]*Institute of Problems of Chemical Physics, RAS, Chernogolovka 142432, Russia. E-mail: bazhen@cat.icp.ac.ru, yagubski@icp.ac.ru*
[b]*Institute of Solid State Physics, RAS, Chernogolovka 142432, Russia*
[c]*Shubnikov Institute of Crystallography of Federal Scientific Research Centre "Crystallography and Photonics", RAS, Moscow, Russia. E-mail: mirsa@list.ru*
[d]*Lomonosov Moscow State University, Moscow 119991, Russia*
[e]*National University of Science and Technology "MISiS", Moscow 119049, Russia*
[f]*Kirchhoff Institute for Physics, Heidelberg University, 69120 Heidelberg, Germany. E-mail: lena.spillecke@kip.uni-heidelberg.de*
[g]*Centre for Advanced Materials (CAM), Heidelberg University, 69120 Heidelberg, Germany*
[h]*National Research South Ural State University, Chelyabinsk 454080, Russia*

†Electronic supplementary information (ESI) available: Fig. S1–S21 and Tables S1–S10. CCDC 2015517–2015519. For ESI and crystallographic data in CIF or other electronic format see DOI: 10.1039/D0DT03092A

elements).[6] In this context, the planar pentadentate N_3O_2 Schiff-base ligands implement the so-called ligand approach toward high magnetic anisotropy by means of optimizing the local atomic coordination of the magnetic ion. Experimental and theoretical studies show that many seven-coordinate metal centers with a PBP geometry are promising anisotropic spin carriers.[1a,2a,4b,7] Considerable efforts in this field in the last few years have resulted in numerous 3d, 4d, 5d and 4f PBP complexes,[1d,e,2c,3b,8] among which of special note are novel 4d and 5d seven-coordinate PBP complexes, the first Mo(III) complex with an open acyclic ligand, $[Mo(DAPBH)Cl_2]^-$,[8b] and a heptacyanide W(IV) complex, $[W(CN)_7]^{3-}$.[8c] The seven-coordinate complexes with 2,6-diacetylpyridine-based open acyclic ligands (N_3O_2) are currently synthesized with all 3d metals,[3] except vanadium. The latter fact presents a clear gap in this research field because vanadium complexes with these ligands are of interest as efficient magnetic building blocks providing strong spin coupling with other spin carriers due to diffuse 3d magnetic orbitals inherent to early transition metal ions.[9] Thus, Prussian blue analogues based on V^{2+} and Cr^{3+} ions reveal bulk magnetic ordering above room temperature.[10] Besides, vanadium complexes can provide significant magnetic anisotropy associated with large zero-field splitting (ZFS) of the ground spin state with axial components $|D|$ up to 20 cm^{-1}.[11]

Given these considerations, we attempted to obtain PBP vanadium complexes with pentadentate N_3O_2 Schiff base ligands. Herein, we report the synthesis of the first seven-coordinate V(III) *trans*-complexes with pentadentate (N_3O_2) 2,6-diacethylpyridine-bis(benzoyl hydrazone) ligand in the various charge states (H_2DAPBH^0, $HDAPBH^{1-}$, $DAPBH^{2-}$): $[V(H_2DAPBH)Cl_2]Cl{\cdot}C_2H_5OH$ (**1**), $[V(HDAPBH)(NCS)_2]{\cdot}0.5CH_3CN{\cdot}0.5CH_3OH$ (**2**) and $[V(DAPBH)(CH_3OH)_2]Cl{\cdot}CH_3OH$ (**3**). We describe the crystal structures and dc magnetic properties of **1–3**; for complex **3**, we also present results of the high-frequency and high-field electron paramagnetic resonance (HF-EPR) study. The obtained experimental results are supplemented with theoretical analysis, which indicates that the magnetic behavior of **1–3** cannot be described in terms of the single-ion ZFS model due to the presence of noticeable spin coupling between V(III)-centers. The latter fact is rather surprising, considering the isolated character of the $[V(DAPBH)X_2]$ units and the large spacing (>7.5 Å) between V^{3+} ions.

Experimental

Materials and methods

2,6-Diacetylpyridine, benzoylhydrazine, VCl_2 (anhydrous), $VCl_3{\cdot}6H_2O$, and NH_4CNS were purchased from commercial sources and used without further purification. Methanol was dried upon refluxing with magnesium methoxide followed by distillation. Acetonitrile was refluxed over calcium hydride and then distilled off. All solvents were purged with argon and stored over molecular sieves 3 Å prior to use. All manipulations involving air-sensitive materials (VCl_2) were carried out under an argon atmosphere using the standard Schlenk-line method. Syntheses using V^{3+} compounds as starting materials were performed under aerobic conditions. Elemental analyses were carried out by the Analytical Department Service at the Institute of Problems of Chemical Physics RAS using a Vario MICRO cube (Elementar Analysensysteme GmbH) equipment.

Synthetic procedures

H_2DAPBH (H_2L) ligand. The H_2DAPBH (H_2L) ligand was prepared in a ketone-hydrazine condensation reaction between one equivalent 2,6-diacetylpyridine and two equivalents of benzoylhydrazine in 96% ethanol according to a previously reported procedure.[12] The yield is more than 90%. Found: C, 69.25; H, 5.35; N, 17.5. Calc. for $C_{23}H_{21}N_5O_2$: C, 69.2; H, 5.3; N, 17.5%. FT-IR ν_{max}/cm^{-1}: 3277m, 1660vs, 1603m, 1580m, 1524vs, 1491m, 1450s, 1372m, 1342m, 1271vs, 1188m, 1160m, 1077m, 917s, 812s, 708vs.

$[V(H_2DAPBH)Cl_2]Cl{\cdot}C_2H_5OH$ (1). To a suspension of H_2DAPBH (150 mg, 0.38 mmol) in absolute CH_3CN (10 ml) solid $VCl_3{\cdot}6H_2O$ (100 mg, 0.38 mmol) was added while stirring. The resulting brown mixture was stirred and heated at 70 °C for 1 hour. A gray precipitate was formed during the first 15 minutes of heating, which subsequently completely dissolved. Instead, after about 30 minutes of heating, an abundant green-brown precipitate began to form. After cooling the reaction mixture, the precipitate was filtered and dissolved in a mixture of CH_3OH/CH_3CN = 1. The resulting solution was filtered, C_2H_5OH (10% by volume) was added to it and it was left to crystallize at room temperature. Two days later, the formation of dark crystals suitable for X-ray diffraction analysis was observed. Yield: 103 mg, 45%. Found: C, 49.5; H, 4.5; N, 11.6. Calc. for $VC_{25}H_{27}N_5O_3Cl_3$: C, 49.8; H, 4.5; N, 11.6%. FT-IR ν_{max}/cm^{-1}: 3409m, 3370m, 1599vs, 1565vs, 1487vs, 1435m, 1322vs, 1276s, 1178s, 1078m, 1024s, 714vs, 684s.

$[V(HDAPBH)(NCS)_2]{\cdot}0.5CH_3OH{\cdot}0.5CH_3CN$ (2). A solution of NH_4SCN (40 mg, 0.5 mmol) in 5 ml of CH_3OH was added to a solution of $[V(H_2DAPBH)Cl_2]Cl{\cdot}C_2H_5OH$ (60 mg, 0.1 mmol) in 7 ml of CH_3OH/CH_3CN mixture while stirring. The resulting reaction mixture was continuously stirred for 1 hour at r.t. and was then filtered. Black block crystals suitable for single-crystal X-ray diffraction were formed after 2 days at room temperature. The mother liquor was decanted and the crystals were washed with diethyl ether and dried under vacuum. Yield: 32 mg, 53% based on the $[V(H_2DAPBH)Cl_2]Cl{\cdot}C_2H_5OH$ complex. Found: C, 52.6; H, 4.25; N, 17.1; S, 10.35. Calc. for $V_2C_{53}H_{47}N_{15}O_5S_4$: C, 52.9; H, 3.9; N, 17.5; S, 10.6%. FT-IR ν_{max}/cm^{-1}: 2065vs (NCS), 1609s, 1572m, 1543m, 1502s, 1389s, 1160 m, 709s, 689s.

$[V(DAPBH)(CH_3OH)_2]Cl{\cdot}CH_3OH$ (3). To a suspension of H_2DAPBH (164 mg, 0.41 mmol) in absolute methanol (10 ml) solid VCl_2 (50 mg, 0.41 mmol) was added under an Ar atmosphere while stirring. The resulting brown mixture was stirred and heated at 50 °C for 1 hour. The ligand was slowly dissolving during this time. The reaction mixture was cooled to room temperature and then filtered. After 2 days of storage of the solution at −18 °C, the formation of dark brown crystals

suitable for X-ray diffraction analysis was observed. The substance was collected by filtration, washed with diethyl ether, and dried under vacuum. Yield: 129 mg, 56%. Found: C, 53.95; H, 5.5; N, 12.0. Calc. for $VC_{26}H_{31}N_5O_5Cl$: C, 53.8; H, 5.35; N, 12.1%. FT-IR ν_{max}/cm^{-1}: 2976w, 2756s, 1588m, 1554m, 1512s, 1386vs, 1160s, 1054s, 1005s, 703s, 685s.

X-ray data collection, structure solution and refinement

X-ray single crystal diffraction data were collected at 150 K on an Oxford Diffraction Gemini-R CCD diffractometer equipped with an Oxford cryostream cooler [λ(MoK$_\alpha$) = 0.71073 Å, graphite monochromator, ω-scans]. Data reduction with empirical absorption correction of experimental intensities (Scale3AbsPack program) was made with the CrysAlisPro software.[13]

The structures were solved by a direct method and refined by a full-matrix least squares method using the SHELX-2016 program.[14] All non-hydrogen atoms were refined anisotropically. The H-atoms were refined in a riding model with isotropic displacement parameters depending on U_{eq} of the connected atom. The N–H and O–H bond distances were refined, with additional geometrical restraints (SADI/DFIX) applied in some cases.

Main crystal and experimental data for **1–3** are listed in Table 1.

Physical measurements

The IR spectra. The IR spectra were measured on solid samples using a PerkinElmer Spectrum 100 Fourier Transform infrared spectrometer in the range of 4000–500 cm^{-1}.

The measurements of temperature and magnetic field dependence of magnetization. The measurements of temperature and magnetic field dependence of magnetization were performed using the vibrating sample magnetometer (VSM) option of the "Quantum Design" physical properties measurements system PPMS – 9 T. The data were corrected for diamagnetic contribution calculated as a sum of Pascal constants. Direct current (dc) magnetization measurements down to 400 mK were performed by means of a commercial MPMS3 SQUID magnetometer from Quantum Design equipped with a ^{3}He insert.

High-frequency/high-field electron paramagnetic resonance (HF-EPR) measurements. High-frequency/high-field electron paramagnetic resonance (HF-EPR) measurements were performed by means of a commercial millimeterwave vector network analyzer (MVNA) from ABmm as a phase sensitive microwave source and detector.[15] The spectra were obtained in the frequency range between 50 GHz and 500 GHz in external magnetic fields up to 16 T. The temperature control between 2 K and 160 K was ensured by using a variable temperature insert (VTI) with a ^{4}He gas flow cryostat from Oxford Instruments. The loose powder samples were placed inside a brass ring in a home-made transmission type EPR probe with no extra glue or grease to align the crystallites with respect to the external magnetic field direction. In order to ensure alignment of the loose powder, the maximum magnetic field of 16 T was applied prior to the measurements and the alignment was monitored by using corresponding orientation jumps in the transmitted microwave signal. Rearrangement of the crystallites to a non-aligned situation was avoided by restricting the magnetic field to a range between 0.2 T and 16 T. For fixed powder measurements, the material was thoroughly ground and then fixed with eicosane. Analysis and simulation of the HF-EPR data as well as that of the low-temperature magnetization data was done by means of the EasySpin software package.[16] *Ab initio* density functional theory (DFT) calculations of the *g*-tensor anisotropy were performed using a spin unrestricted self-consistent field method (SCF)[17] with B3LYP hybrid functionals and a SVP[18] basis set for all electrons as implemented in the ORCA software package.[19,20]

Table 1 Crystal data and structural refinement parameters for complexes **1–3**

	1	2	3
Chemical formula	$C_{25}H_{27}Cl_3N_5O_3V$	$C_{26.5}H_{23.5}N_{7.5}O_{2.5}S_2V$	$C_{26}H_{31}ClN_5O_5V$
Formula weight	602.80	602.09	579.95
Cell setting	Orthorhombic	Orthorhombic	Monoclinic
Space group, *Z*	$P2_12_12_1$, 4	$P2_12_12_1$, 8	$P2_1/c$, 4
Temperature (K)	150(1)	150(1)	150(1)
a (Å)	7.29023(8)	13.9738(2)	19.5934(3)
b (Å)	15.3895(2)	14.3549(2)	7.49770(8)
c (Å)	22.8617(3)	27.3124(4)	20.3843(3)
α (°)	90	90	90
β (°)	90	90	112.382(2)
γ (°)	90	90	90
Cell volume (Å^3)	2564.92(5)	5478.66(14)	2768.98(7)
ρ (g cm^{-3})	1.561	1.460	1.391
μ, cm^{-1}	7.38	5.57	4.99
Crystal size, mm^3	0.12 × 0.29 × 0.71	0.06 × 0.08 × 0.53	0.13 × 0.23 × 0.27
Refls collected/unique	21 049/8631	30 256/15 367	27 429/8079
R_{int}	0.0170	0.0173	0.0149
θ_{max} (°)	31.00	29.50	29.00
Parameters refined	340	785	357
Final R_1, wR_2 [$I > 2\sigma(I)$]	0.0301, 0.0819	0.0370, 0.0811	0.0307, 0.0789
Goodness-of-fit	1.002	1.001	1.001
CCDC number	2015517	2015518	2015519

Ligand-field and spin coupling calculations for V(III) complexes. The electronic structure of V(III) complexes **1–3** and their ZFS characteristics were analyzed using the conventional ligand-field (LF) Hamiltonian (eqn (S1), ESI†) in combination with the angular-overlap model (AOM),[21] as described in the ESI.† The spin coupling between two neighboring $[V^{III}(DAPBH)(CH_3OH)_2]$ in **3** units was explored in terms of the many-electron superexchange theory;[22] the computational details are outlined in the ESI.†

Results and discussion

Synthetic considerations

Complexes **1–3** were obtained following the synthetic procedure previously used to obtain the pentagonal-bipyramidal complexes of other 3d metals.[3]

Given the wide range of accessible oxidation states for vanadium, we were interested in the preparation of seven-coordinate complexes of vanadium(II) and (III). Therefore, the simple salts of V^{2+} and V^{3+}, anhydrous VCl_2, and hexahydrate $VCl_3{\cdot}6H_2O$ were used as the starting compounds.

We note here that regardless of the oxidation state (+2 or +3) in the initial vanadium salt used for the synthesis, it was not possible to obtain the seven-coordinate vanadium(II) complex by the direct reaction. Attempts with some additional precautions (namely, the reaction in aprotic solvents and oxygen-free conditions and the reaction in the presence of a dithionite reducing agent) failed to produce the V^{2+} complex. A complex of trivalent vanadium was always formed. Apparently, this is due to the presence of non-innocent C=N bonds capable of oxidizing V^{2+} to V^{3+}.

The interaction of $VCl_3{\cdot}6H_2O$ with the H_2DAPBH ligand leads to the formation of $[V(H_2DAPBH)Cl_2]Cl{\cdot}C_2H_5OH$ (**1**). The compound contains a neutral unaltered protonated equatorial ligand, Cl^- ions in axial positions (Fig. 1a), and a chlorine anion in the external coordination sphere. The Cl^- ions in the axial positions can be easily replaced, for example, with NCS^- groups by the treatment of the $[V(H_2DAPBH)Cl_2]Cl{\cdot}C_2H_5OH$ **1** complex solution with an excess of NH_4NCS. In this case, the neutral complex $[V(HDAPBH)(NCS)_2]{\cdot}0.5CH_3CN{\cdot}0.5CH_3OH$ (**2**) is formed. The complex contains the monodeprotonated, mononegative ligand $HDAPBH^-$ in the equatorial, and two NCS^- anions in the apical positions (Fig. 1b).

When using the divalent vanadium salt (VCl_2) as a starting compound in methanol under an inert atmosphere, the interaction with the H_2DAPBH ligand also leads to a V(III) complex, $[V(DAPBH)(CH_3OH)_2]Cl{\cdot}CH_3OH$ (**3**). In this complex, the equatorial ligand is completely deprotonated, the methyl alcohol molecules occupy the axial positions (Fig. 1c), and the chlorine anion is located in the outer coordination sphere. As we have already noted, the formation of trivalent vanadium is associated with the oxidation of initial V^{2+}, a strong reducing agent, with the ligand—the Schiff base H_2DAPBH, containing the unsaturated C=N bonds. Complexes **1–3** are stable in air at room temperature both in the solid state and in solutions.

Description of the crystal structures of 1–3

Complex **1** crystallizes in the orthorhombic space group $P2_12_12_1$. The asymmetric unit includes the $[V(H_2DAPBH)Cl_2]^+$ cation, Cl^- anion and ethanol solvent molecule, all in general positions. An ORTEP drawing of **1** is shown in Fig. S2.† Complex **2** crystallizes in the orthorhombic space group $P2_12_12_1$ as complex **1**, but these two compounds are not isostructural (see Table 1). There are two $[V(HDAPBH)(NCS)_2]$ neutral molecules, one acetonitrile molecule and one methanol molecule in the asymmetric unit, all in general positions (Fig. S4†). One NCS^- ligand and both solvent molecules are statistically disordered between two sites with the same 0.7/0.3 occupancy ratio for NCS^- and CH_3OH and 0.5/0.5 occupancy ratio for CH_3CN. Complex **3** crystallizes in the monoclinic space group $P2_1/c$. The asymmetric unit includes the $[V(DAPBH)(CH_3OH)_2]^+$ cation, Cl^- anion and methanol solvent molecule, all in general positions (Fig. S6†). Key bond distances and angles in the structures of **1**, **2** and **3** are listed in Tables S1, S3 and S5,† respectively.

Compounds **1–3** contain vanadium(III) complexes with pentadentate ligands of various degrees of protonation and charges: $[H_2DAPBH]^0$ in **1**, $[HDAPBH]^-$ in **2** and $[DAPBH]^{2-}$ in **3** (Fig. 1). The local coordination geometry around the V(III) center corresponds to a distorted pentagonal bipyramid. V(III) is surrounded by three N and two O atoms of the pentadentate

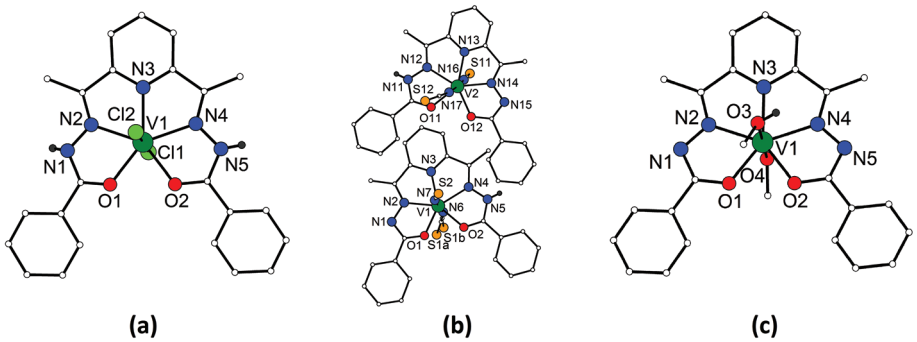

Fig. 1 Molecular structures of **1** (a), **2** (b) and **3** (c). Counter anions, lattice solvents and non-acidic H atoms are omitted for clarity.

ligand in the equatorial plane. Two axial coordination sites are occupied by Cl^- anions in the structure of **1**, N atoms of NCS^- anions in **2** and O atoms of neutral methanol molecules in **3**. The structural analysis reveals different degrees of planarity of the pentadentate ligands in **1–3**. The maximal deviation from the planarity is observed for the fully protonated ligand $[H_2DAPBH]^0$ in **1**, whereas the doubly deprotonated ligand $[DAPBH]^{2-}$ in **3** is almost planar. The dihedral angle between two semi-carbazone planes of the ligand defined by 7 non-metallic atoms of two pentagonal cycles (for example, O1, C7, N1, N2, C9, C10, N3 and O2, C17, N5, N4, C15, C14, N3 in Fig. 2) is 13.93(5)° in **1**, 7.90(8) and 11.00(8)° in **2** and only 3.76(3)° in **3**. A side view of the complexes demonstrates noticeable deviation of phenyl and pyridine cycles from the central VN_3O_2 plane for the $[H_2DAPBH]^0$ ligand in **1** (Fig. 3, left) in contrast to the almost ideal planarity of the $[DAPBH]^{2-}$ ligand in **3** (Fig. 3, right).

Deprotonation is followed by noticeable changes in the geometry of the VN_2CO/VN_2HCO cyclic groups involved in the central chelating node of the pentadentate ligand. The bond length values in **1–3** in the protonated VN_2HCO and deprotonated VN_2CO cycles are compared in Tables 2 and 3.

In the deprotonated VN_2CO cycle, the V–N, V–O, C–N bonds are shorter while the C–O bonds are longer as compared with similar bonds in the protonated VN_2HCO cycle. This is illustrated in Fig. 2 for one of two independent $[V(HDAPBH)(NCS)_2]$ complexes in the structure of **2**.

In order to compare the degree of deviation from the ideal pentagonal bipyramidal coordination of the metal centers in a more unified way, we performed calculations of continuous shape measures by using SHAPE (2.1) program.[23] The calculation results listed in Table S7† show the minimum deviation for compound **3**. The analysis also confirms small but meaningful variations for two symmetry-independent molecules in the unit cell of **2**.

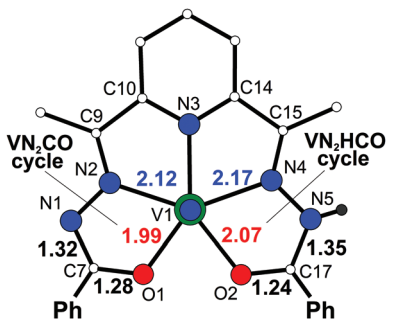

Fig. 2 Comparison of bond length values (Å) in the VN_2CO and VN_2HCO cycles of the V complex with the $[HDAPBH]^-$ ligand in **2**.

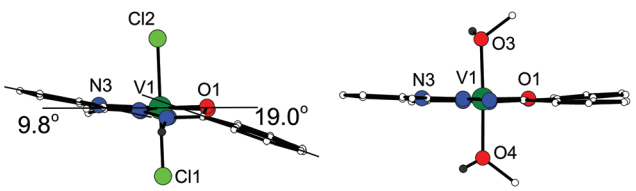

Fig. 3 Side view of the V(III) complexes in **1** (left) and **3** (right). Dihedral angles between pyridine and phenyl planes and the central VN_3O_2 plane in **1** are shown.

Table 2 Bond lengths (Å) in the protonated VN_2HCO cycles of V(III) complexes **1** and **2** with H_2DAPBH^0 and $HDAPBH^-$ pentadentate ligands, respectively

	1	**1**	**2**, V(1) center	**2**, V(2) center
Complex charge	1+	1+	0	0
Ligand charge	0	0	1−	1−
V–N	2.140(2)	2.153(2)	2.166(2)	2.173(2)
V–O	2.059(2)	2.061(2)	2.067(2)	2.114(2)
C–N	1.352(3)	1.348(3)	1.350(4)	1.353(3)
C–O	1.249(2)	1.249(2)	1.239(3)	1.247(3)

Table 3 Bond lengths (Å) in the deprotonated VN_2CO cycles of V(III) complexes **2** and **3** with $HDAPBH^-$ and $DAPBH^{2-}$ pentadentate ligands, respectively

	2, V(1) center	**2**, V(2) center	**3**	**3**
Complex charge	0	0	1+	1+
Ligand charge	1−	1−	2−	2−
V–N	2.123(2)	2.114(2)	2.1524(9)	2.1473(10)
V–O	1.993(2)	2.008(2)	2.0109(8)	2.0193(8)
C–N	1.316(3)	1.316(3)	1.3212(14)	1.3147(15)
C–O	1.282(3)	1.282(3)	1.2889(13)	1.2892(14)

The crystal packing of **1–3** is determined by hydrogen bonding. The NH-groups of the pentadentate ligands are locked on the Cl^- anion and O atom of the ethanol solvent in **1**, S atom of the SCN^- ligand and N atom of the acetonitrile solvent in **2**. In **3**, in the absence of the NH proton, OH···Cl hydrogen bonds are formed between the axial methanol ligands and the Cl^- anions (see Fig. S3, S5, S7 and Tables S2, S4, S6, ESI† for hydrogen bond geometry). Besides, a π-stacking between the pentadentate ligands of adjacent complexes is found in all three structures. It is especially strong in **1** where V-complexes form layers parallel to the *ab* plane (Fig. 4a). The nearest V···V distance is 7.2902(5) Å along *a* between the cations connected by hydrogen bonds $N–H_{H_2DAPBH}···O–H_{EtOH}···Cl_{ligand}$ through the ethanol bridge (interaction 1 in Fig. 4a). The average planes of the H_2DAPBH ligands are not parallel within the layer: the corresponding dihedral angle between the VN_3O_2 planes is 29.76(3) °. However, the phenyl and pyridine cycles are not in the central VN_2O_2 plane (Fig. 3, left) that allows them to pack almost parallel to each other along *a* and form a lot of shortened C···C contacts less than the sum of van der Waals radii (3.6 Å) which are shown in Fig. 4a by thin dotted lines. The V···V distances are 8.1084(5) and 9.1259(5) Å for the π-stacking interactions **2** and **3**, respectively.

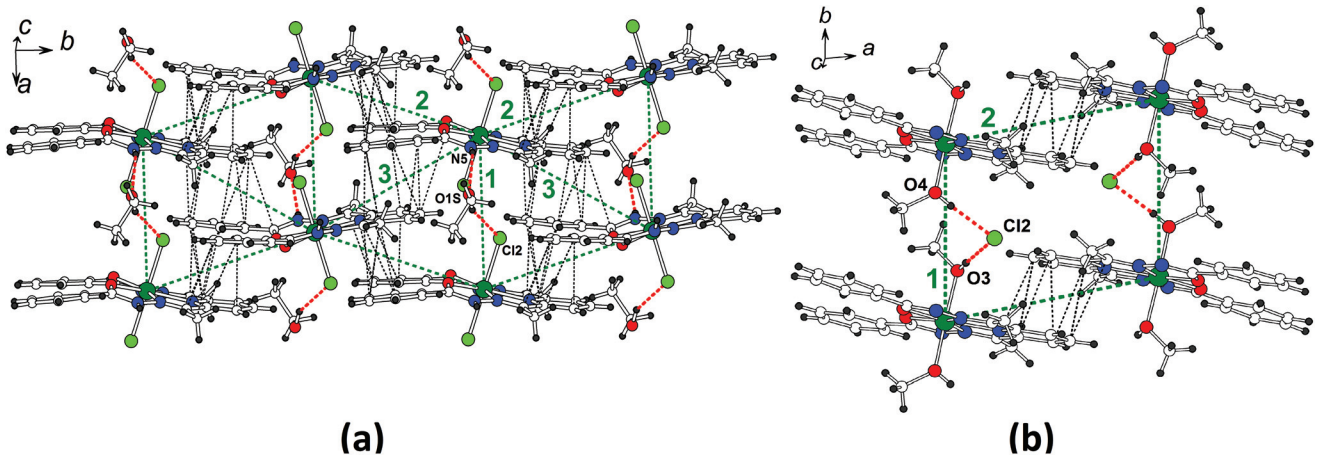

Fig. 4 The *ab* layers in structures **1** (a) and **3** (b) with hydrogen bonding and π-stacking interactions. Hydrogen bonds from acidic H-atoms (red dashed lines, H-bond geometry is given in Tables S2 and S6†), C···C contacts <3.6 Å (black dotted lines), V···V distances (green dashed lines, (a): 1 = 7.2902(5), 2 = 8.1084(5), 3 = 9.1259(5) Å, (b): 1 = 7.4977(2), 2 = 8.6545(6) Å) are shown.

In the structure of **3**, the V(III) complexes also form layers parallel to the *ab* plane (Fig. 4b). The doubly deprotonated DAPBH ligands are essentially flat (Fig. 3, right) and parallel within the layer. The nearest V···V distance in **3** is 7.4977(2) Å along *b* in the infinite chains of the V(III) complexes interacting *via* O–H_{ligand}···Cl_{anion}···H–O_{ligand} hydrogen bonds (interaction 1). The adjacent chains along *a* are paired through a π-stacking of the ligands (interaction 2), and the V···V distance is 8.6545(6) Å. Intermolecular interactions in **2** are described in the ESI (Fig. S5†).

In order to rationalize the molecular structure of **1–3**, we performed density functional theory (DFT) calculations for isolated complexes using the ORCA 3.0.3 suite of programs and employing the spin-unrestricted method at the B3LYP/SVP(TzVPP) level of theory.[19,20] The DFT-optimized geometry of **1–3** is shown in Fig. S8–S10, ESI;† these results well reproduce the aforementioned structural features of **1–3**. Interestingly, DFT calculations indicate that the non-planar structure of the mono- and doubly protonated H_xDAPBH^{2-x} ligands (x = 1, 2) is mainly due to rotations of the phenyl rings caused by repulsion between the proton of the NH group and the nearest proton of the phenyl group (separated by the distance of ≈2.2 Å, Fig. S8 and S9, ESI†). In the absence of this repulsion in the fully deprotonated ligand $DAPBH^{2-}$, DFT calculations result in a perfectly planar structure of **3** with two coplanar phenyl rings (Fig. S10, ESI†), in agreement with the X-ray structural data (Fig. 3, right).

DC magnetic susceptibility studies

The magnetic susceptibility was measured on the polycrystalline samples of complexes **1–3** in the temperature range of 2.0–300 K under the applied magnetic field of 0.1 T; the χT *vs.* T plots are shown in Fig. 5a–c. The χT value at room temperature approaches 1.0 $cm^3\ mol^{-1}$ K, which is expected for V(III) with S = 1 and g = 2. The χT product gradually decreases upon cooling to ~30 K, and then it rapidly drops to *ca.* 0.35 $cm^3\ mol^{-1}$ K at a low temperature (Fig. 5a–c).

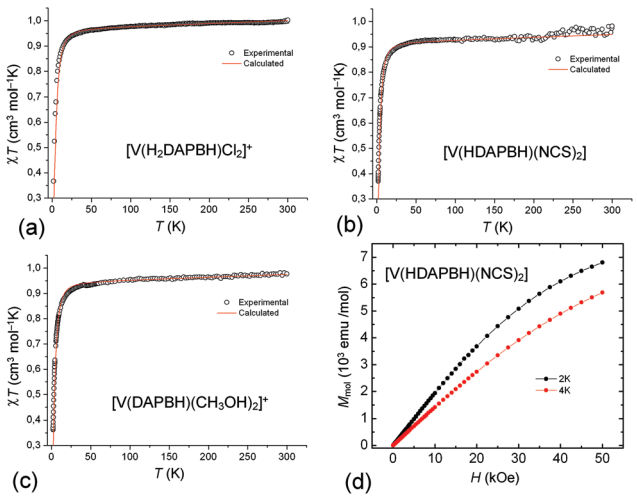

Fig. 5 (a)–(c) χT *versus* T at 0.1 T for complexes **1–3**, experimental (open circles) and calculated with the ZFS model (solid red lines), (d) M_{mol} *versus* H at 2 K and 4 K for **2**. The solid lines are a guide for the eye. The fitted $M_{mol}(H)$ curves for **3** are shown in Fig. S14, ESI.†

At first glance, it is natural to attribute such magnetic behavior to a free or weakly coupled S = 1 spin system with a positive zero-field splitting (ZFS) parameter D, considering that the large spacing between magnetically isolated V(III) ions encapsulated in bulk [V(HDAPBH)X_2] complexes should prevent magnetic coupling in **1–3**. Following this idea, we performed a primary analysis of the magnetic susceptibility χT of **1–3** in terms of the single-ion ZFS spin Hamiltonian (SH):

$$H = g\mu_B \boldsymbol{BS} + D\left(S_z^2 - S(S+1)/3\right) + E\left(S_x^2 - S_y^2\right) + H_{TIP} \quad (1)$$

where D and E are, respectively, the axial and rhombic ZFS parameters, μ_B is the Bohr magneton, g is the Landé factor of V(III), $\boldsymbol{B}$ is the magnetic induction and H_{TIP} is the second-order paramagnetic temperature-independent term. The best agree-

ments with the experimental data are obtained at D = +11.0, E = 1.7 cm^{-1}, g = 1.965, χ_{TIP} = 1.16 × 10^{-4} cm^3 mol^{-1} for **1**, D = +8.9, E = 0.2 cm^{-1}, g = 1.913, χ_{TIP} = 1.12 × 10^{-4} cm^3 mol^{-1} for **2** and D = +10.1, E = 0.4 cm^{-1}, g = 1.940, χ_{TIP} = 1.12 × 10^{-4} cm^3 mol^{-1} for **3**; the simulated χT curves are shown in solid red lines in Fig. 5a–c. It is also noteworthy that the magnitude of the calculated ZFS parameter D in **1–3** is reasonably consistent with the D values observed in many other V(III) complexes.[11] These calculations indicate that the ground state of vanadium (III) PBP complexes **1–3** is a spin-only triplet spin state (S = 1) with two unpaired electrons on the two lowest $3d_{xz}$ and $3d_{yz}$ orbitals (Tables S6, S7 and Fig. S11, ESI†). The presence of considerable ZFS of the ground spin state S = 1 with positive D is evidenced experimentally by the fact that at low temperatures, magnetization M_{mol} does not saturate even in a strong magnetic field (50 kOe, Fig. 5d).

However, although these preliminary single-ion simulations are well consistent with the experiment (Fig. 5), further analysis indicates a more complicated nature of magnetism in **1–3**, which is beyond the pure single-ion ZFS model. Namely, below we show that high-frequency EPR measurements for complex **3** reveal a significantly lower ZFS parameter ($D \approx$ +4.5 cm^{-1}) and, rather unexpectedly, the presence of a noticeable dimer-like antiferromagnetic (AF) spin coupling between distant V(III) ions. The origin of these findings is well explained by our theoretical analysis based on superexchange calculations and ligand-field calculations (see the next sections).

HF-EPR spectroscopy

In order to obtain straightforward information on the ZFS parameters and to elucidate the basic magnetic interactions underlying the magnetic behavior of V(III) PBP complexes **1–3**, we have undertaken a high-frequency/high-field electron paramagnetic resonance (HF-EPR) study for compound **3**. The HF-EPR measurements were performed on loose and fixed powder samples of complex **3**. For both preparation techniques, the measured resonance spectra exhibit clearly resolvable features as can be seen in Fig. 6. The obvious differences between the shown spectra measured at approximately the same frequencies on the loose and fixed powder sample prove proper alignment of the loose powder in the external magnetic field. Both spectra exhibit some mixing of phase and amplitude information, which is due to the applied measurement technique and was included as a parameter in the corresponding simulations displayed as red lines, respectively.

The temperature dependence of the loose powder spectra of **3** at a constant frequency of 396.2 GHz (Fig. 7, left) implies that the pronounced low-temperature feature is associated with a ground state transition. In addition, while at T = 2 K only one main feature is visible, an excited feature appears on the high field site of the main one with increasing temperatures.

Tuning the microwave frequency allows determining the magnetic field dependence of the resonance features. The corresponding resonance frequency *vs.* the magnetic field diagram for the loose powder of complex **3** is shown in Fig. 8.

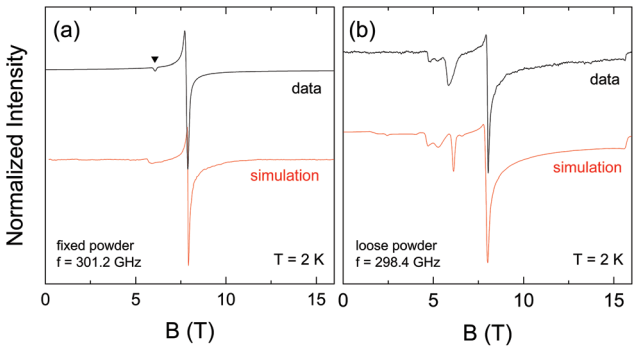

Fig. 6 HF-EPR spectra (black lines) of aligned loose powder (a) and fixed powder (b) of complex **3** measured at T = 2 K and a fixed frequency of 301.2 GHz and 298.4 GHz, respectively. The black triangle indicates an extra feature as discussed in the text. The red lines correspond to a simulation using the SH (eqn (1)) with the parameters listed in Table 4.

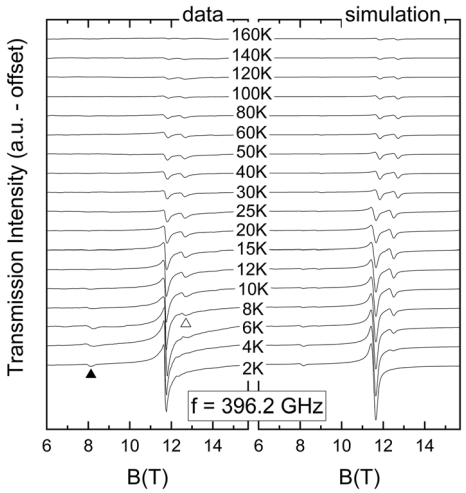

Fig. 7 (Left) HF-EPR spectra for an aligned loose powder sample of **3** at f = 396.2 GHz at various temperatures between 2 K and 160 K. The data are vertically shifted for clarity. A weak feature arising from a forbidden transition (see the text) at T = 2 K and an excited one are indicated by filled and open triangles, respectively. (Right) Corresponding simulation using the SH in eqn (1) and the parameters listed in Table 4.

At T = 2 K, there is one main branch shown by black squares in Fig. 8 and in Fig. S11, ESI.† The branch features a ZFS of around 180 GHz and pronounced bending in the low-field regime, while linear behavior corresponding to a g-factor of ≈2 is found at high magnetic fields. Measurements at higher temperatures (10 K–15 K) show the appearance of additional resonance branches, which are associated with several excited features. The main feature of the spectra displayed in Fig. 6a and the presence of a single resonance branch at T = 2 K are explained in terms of the single-ion ZFS model for an anisotropic S = 1 system. The observed pronounced bending of the low-temperature branch in the low-field regime confirms the proper alignment of the crystallites perpendicular to the external field direction and a positive sign for the axial crystal field anisotropy parameter D can be read-off.[24,25] However, the

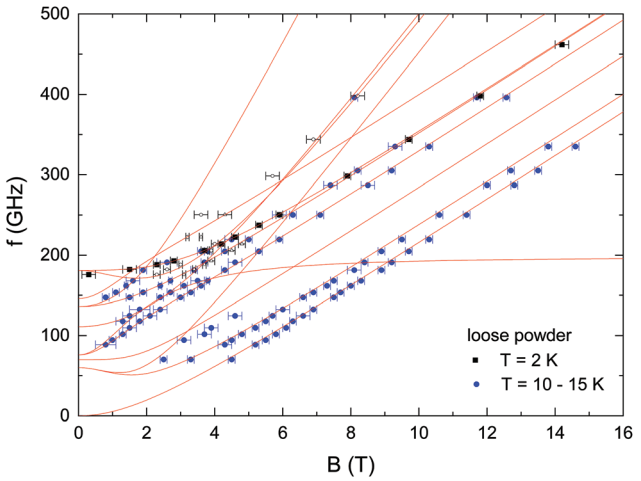

Fig. 8 Magnetic field dependence of the resonance frequencies for a loose powder sample of **3**. Black squares correspond to measurements at T = 2 K and blue dots correspond to thermally activated features at T = 10 K. The red lines show a simulation of the resonance branches using the SH in eqn (1) with the parameters listed in Table 4. For the sake of simplicity, only the simulated branches that correspond to the observed transitions are shown. Open small symbols display weak features showing up in the spectra obtained at T = 2 K that are arising from forbidden or excited transitions.

appearance of thermally excited branches as shown in Fig. 7 and 8 (the black open triangle in Fig. 7) is not predicted by simple models of non-interacting V(III)-centers. Instead, the data suggest the presence of finite intermolecular spin coupling between neighboring metal centers.[26] The corresponding spin Hamiltonian transforms to

$$H = \mu_B \boldsymbol{B}\boldsymbol{g}\boldsymbol{S} + D\left(S_z^2 - S(S+1)/3\right) + E(S_x^2 - S_y^2) - J\boldsymbol{S}_1\boldsymbol{S}_2 \quad (2)$$

where the first term describes anisotropic Zeeman interaction of the spin S with the external magnetic field, B, D and E are ZFS parameters, and the last term covers the magnetic interaction between two neighboring spins S_1 and S_2 with the exchange parameter J. In general, the g-tensor exhibits three components g_x, g_y and g_z. From the axial structure of the molecule, we assume axial symmetry for the g-tensor so that it can be simplified to axial ($g_{||}$) and transversal ($g_\perp$) components. This is supported by our ligand-field (LF) calculations for **1–3** combined with the angular overlap model[21] (see the ESI† for computational details), evidencing the uniaxial character of the ZFS tensor, for example, $D \approx +4$, E = 0.035–0.09 cm^{-1} (Table S10, ESI†). Employing this model allows one to simulate the resonance branches shown in Fig. 8 and Fig. S12† as well as the spectra shown in Fig. 6 and 7. The results show that the experimental data on both loose and fixed powder samples are well described by the simulation using the SH in eqn (2). The resulting SH parameters are listed in Table 4.

Our analysis shows that powder spectra are well described by assuming well aligned molecules with $g_\perp \perp \boldsymbol{B}_{ext}$. Associating the loose powder spectra with the response of aligned molecules is further confirmed when all resonance branches

Table 4 SH parameters obtained from simulations of the resonance frequency *vs.* field dependence of the loose and fixed powder sample shown in Fig. 8 and S12.† These parameters were used to simulate the spectra shown in Fig. 6 and 7. The third column shows calculated g-values

SH parameter	Simulation results	Calculated parameters[a]
$g_{\|\|}$	1.97(2)	1.9715834, 1.9722007
$g_\perp$	1.99(2)	1.9984610
D	+136(3) GHz (4.5(1) cm^{-1})	—
E	0(1) GHz	—
J	−34(3) GHz (−1.1(1) cm^{-1})	—

[a] DFT calculations.

observed in the fixed, *i.e.*, randomly aligned powder are considered (see Fig. S12, ESI†). While all resonance branches in Fig. S12† are explained by the model, a comparison with the simulation shows that the branches that are also observed in the loose powder indeed correspond to the ones with $g_{||} \perp B_{ext}$.

Our finding of D being much larger than J allows sketching the anisotropy effects by means of a monomer picture: the positive sign of D implies zero field splitting of the triplet states with m_S = 0 being the ground state, *i.e.*, planar anisotropy without significant in-plane anisotropy. These results are well consistent with our LF calculations ($D \approx +4$ cm^{-1}, $E \ll D$, Table S10, ESI†). While loose powders are hence aligned so that $g_{||} \perp B_{ext}$, rotational symmetry ($g_x = g_y$ and $E \approx 0$) implies that there is no preferential direction within the xy-plane so that the observed single feature can be straightforwardly attributed to the transversal direction. These conclusions are well corroborated by our calculations of the angular dependence of magnetization for the isolated $[V(DAPBH)(CH_3OH)_2]^+$ molecule, which show a distinct easy-plane nature of magnetization (Fig. S16, ESI†) and the absence of magnetic anisotropy in the equatorial xy plane (at B_{ext} || xy, Fig. S17, ESI†). The presence of two molecules within one unit cell in general allows for different directions of the respective easy anisotropy plane, which may be misaligned by the angle 2φ between both molecules. In a loose powder measurement, this implies the alignment of the crystallites perpendicular to the effective anisotropy axis so that the external magnetic field is misaligned by φ to the xy-plane of the molecular anisotropy. However, as demonstrated in Fig. S13,† where the field dependence of the ground state transition is simulated for different angles φ, such misalignment would lead to a splitting of the branch observed at low temperatures. A comparison of the simulation with the experimental data implies that the angle between the crystal field axes of the two molecules in the unit cell is smaller than 10°, while the best simulation of the branch is obtained for φ = 0°. Hence, the crystal field axes for all molecules are almost perfectly aligned. This result is corroborated by the simulation of the fixed powder studies.

Our analysis implies that the thermally excited resonance feature is attributed to the effect of dimer-like antiferromagnetic coupling between two neighboring vanadium centers; its origin is analyzed below in terms of superexchange

calculations between the $[V(DAPBH)(CH_3OH)_2]^+$ units (see the next section). Estimating dipolar interactions[27] between $S = 1$ centers separated by about 7.5 Å yields magnetic coupling in the range of $J_{dipolar} \sim 0.2$ GHz, which is much too small to account for the observed separation of the extra feature from the main one and its temperature dependence.[28] The small feature showing up in the loose powder spectra marked by a black filled triangle in Fig. 6a is a forbidden transition, *i.e.*, it is associated with a change of spin state $\Delta m_s = \pm 2$. In general, forbidden transitions are not supposed to be detected for $E = 0$ and aligned crystallites but for higher order transverse terms, the presence of mixed modes of microwave radiation or various molecular orientations in the unit cell may account for forbidden features. Specifically, mode mixing in the transmission-type probe setup implies that not only the conventional perpendicular mode is detected but also the parallel one, which may cause forbidden transitions even in the absence of a transversal anisotropy term.[28,29] A mixture of the microwave modes was hence included as a parameter in all simulations of the spectra. In addition, slight misalignment of molecules at different unit cell positions implies that even in the case of perfect alignment with respect to the crystals' effective anisotropies, misalignment of the individual molecules is present.

The presence of small dimer-like spin coupling is supposed to yield a maximum in the magnetic susceptibility at $T \approx 2$ K and downturn below.[30] This behavior is clearly confirmed by Fig. 9 where low-temperature dc-susceptibility data are presented. The data are well described by a simulation using the SH eqn (2) and employing *g*-values and anisotropy parameters as shown in Table 4 but an antiferromagnetic dimer coupling of −37.5 GHz. This coupling value is within the error range of the value obtained by HF-EPR. In contrast, ignoring intermolecular magnetic interaction but employing the same anisotropy and *g*-values obtained from EPR fails to describe the experimental data. Simulation with $J = -34$ GHz as obtained from the best fit to the EPR data still shows a good qualitative agreement, while the position of the maximum in χ is reproduced best by using $J = -43$ GHz (see Fig. 9). The latter value is however too large to account for the position of the excited features in Fig. 7 and 8.

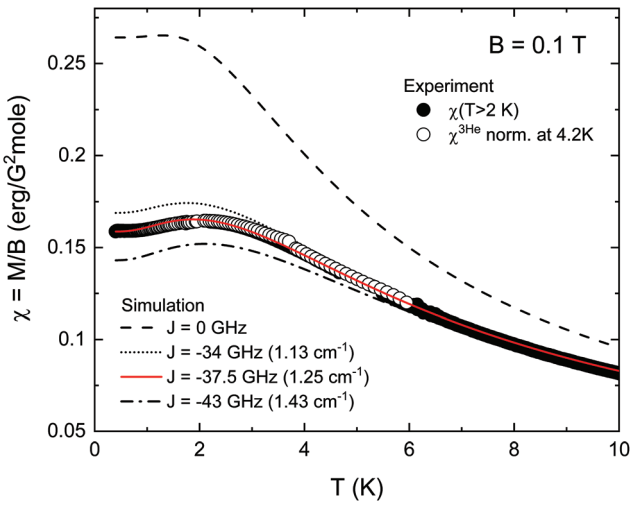

Fig. 9 Temperature dependence of the static magnetic susceptibility of **3** between 0.4 K and 10 K. The data obtained in the ^{3}He-setup on a fixed powder of complex **3** were normalized at 4.2 K to the higher temperature data also shown in this figure. The solid line shows a simulation using SH eqn (2) and the parameters described in the text. For comparison, a simulation using the same SH parameters but with $J = 0$ is given as the dashed line.

It is also important to note that the ZFS model with the isotropic *g*-tensor and with dimer-like antiferromagnetic spin coupling reproduces the experimental χT curve for **3** over the entire temperature range of 2–300 K at $g = 1.950$, $D = +4.6$ cm^{-1}, $E = 0$, $J = -1.1$ cm^{-1} and $\chi_{TIP} = 1.12 \times 10^{-4}$ cm^3 mol^{-1}, Fig. S21, ESI.†

Thus, the dc magnetic data and HF-EPR measurements indicate a positive ZFS energy in **1–3**. In these vanadium(III) PBP complexes, two electrons with parallel spins occupy the two lowest magnetic orbitals, $3d_{xz}$ and $3d_{yz}$ orbitals, to produce a high-spin ($S = 1$) ground state with no first-order orbital momentum (Fig. S15, ESI†). This corresponds to the spin-only case with second-order magnetic anisotropy described by the ordinary ZFS spin Hamiltonian $DS_z^2 + E(S_x^2 - S_y^2)$; our LF/AOM calculations indicate a positive axial anisotropy parameter $D \sim +4$ cm^{-1} and small transverse *E* parameter (Table S10, ESI†). Besides, these calculations show that the orbital composition of the ground-state wave function $\det||3d_{xz}\uparrow, 3d_{yz}\uparrow||$ of V(III) PBP complexes **1–3** is rather insensitive to departures from the strict PBP symmetry D_{5h}. The reason is that the in-plain distortions of the VN_3O_2 pentagon produce a relatively small energy splitting of the two lower 3d orbitals of the V(III) ion, $3d_{xz}$ and $3d_{yz}$ (a few hundreds of cm^{-1}, see Table S8, ESI†), since they interact with the valent 2p orbitals of O and N atoms in the π-bonding mode (Fig. S15, ESI†). As a result, the magnetic behavior of the distorted PBP complexes **1–3** should be close to that of the undistorted $V^{III}(3d^2)$ complex with idealized D_{5h} symmetry; this accounts for the uniaxial character of the magnetic anisotropy of complexes **1–3** (see Table S10, Fig. S16 and S17 ESI†).

Spin coupling calculations

The origin of the long-range dimer-like spin coupling in compound **3** is intriguing considering that its structure is built of isolated complexes with a large spacing between V^{3+} ions (>7 Å, Fig. 4). To get more insight into this problem, we explored the mechanism of superexchange interactions between the $[V(DAPBH)(CH_3OH)_2]^+$ units in **3** in terms of the many-electron superexchange theory[22] (see the ESI† for the theoretical approach and computational details).

An inspection of the molecular structure of **3** shows that it is built of zig-zag chains formed by two vanadium pairs with short (8.65 Å) and long (10.65 Å) V···V distances, in which $[V^{III}(DAPBH)(CH_3OH)_2]^+$ complexes with the coplanar equatorial planes VN_3O_2 are connected *via* the π–π stacking contacts of macrocyclic rings (Fig. S18, ESI†); the shortest distance between the V^{III} centers is 7.5 Å (pair 1, Fig. S18 and

Fig. S19a†). Superexchange calculations indicate that the π-stacking of two DAPBH planar ligands provides the most efficient exchange pathway between spins S = 1 of two V(III) ions, which results in AF spin coupling of J = –0.49 cm^{-1} for the short pair (V···V = 8.65 Å, pair 2 shown in Fig. 10 and Fig. S19b, ESI†) and J = –0.09 cm^{-1} for the long pair (V···V = 10.65 Å, Fig. S20, ESI†).

The underlying reason behind the relatively strong AF spin coupling in pair 2 (8.65 Å) is that the largest matrix element $t_{xz,xz}$ = 136.5 cm^{-1} (eqn (S20)†) is diagonal, which connects two half-filled magnetic orbitals 3d$_{xz}$(A) and 3d$_{xz}$(B) of two vanadium centers (A and B) involved in the two-electron wave function det||3d$_{xz}$↑, 3d$_{yz}$↑|| of the ground state of the V^{III} centers (Fig. 10b). This matrix element measures the efficiency of the indirect overlap of the 3d$_{xz}$(A) and 3d$_{xz}$(B) magnetic orbitals mediated by the ligand's π(*z*)(DAPBH) molecular orbitals that interact through the π-stacking contact of two DAPBH ligands (Fig. 10c). According to the superexchange theory, interaction between two half-filled orbitals leads to AF spin coupling with $J \sim -(t_{xz,xz})^2/U(\mathrm{A} \rightarrow \mathrm{B}) \approx -0.5$ cm^{-1}, where U(A → B) is the charge-transfer energy, typically 5 eV (~40 000 cm^{-1}) for early 3d elements. The exchange parameter of J = –0.49 cm^{-1} obtained from many-electron superexchange calculations (see the ESI† for details) is reasonably consistent with the experimental value (J = –1.1 cm^{-1}); enhanced spin coupling can be due to the diffuse character of the 3d magnetic orbitals of V(III) which often leads to high exchange parameters.[10] Considerably weaker AF spin coupling J = –0.09 cm^{-1} in the long pair (10.65 Å, Fig. S20, ESI†) is caused by a lower efficiency of the π–π stacking in mediating spin coupling due to imperfect overlap of the macrocyclic rings, as can be seen from Fig. S20, ESI.†

On the other hand, the absence of the π-stacking in other vanadium pairs (Fig. S18, ESI†) leads to small matrix elements $t_{\alpha\beta}$ (α,β = xy, $x^2 - y^2$, z^2, xz, yz) and very weak spin coupling. Thus, in the closest vanadium pair with V···V = 7.5 Å (pair 1 in Fig. S19a, ESI†) the diagonal matrix elements $t_{xz,xz}$ and $t_{yz,yz}$ connecting half-filled 3d$_{xz}$ and 3d$_{yz}$ orbitals on vanadium centers A and B (Fig. 10b) are small (10 cm^{-1} or less, eqn (S19)†). As a result, the corresponding AF superexchange pathways in pair 1 are much less efficient than those in pair 2. Moreover, the presence of larger off-diagonal matrix elements connecting the half-filled 3d$_{xz}$ and 3d$_{yz}$ orbitals with empty orbitals (such as $t \sim 40$ cm^{-1} for 3d$_{xz}$ and 3d$_{z^2}$ orbitals, eqn (S19), ESI†) opens up competing ferromagnetic exchange pathways. Ultimately, this leads to a marginally weak spin ferromagnetic coupling of J = +8.4 × 10^{-4} cm^{-1}, which is several orders of magnitude smaller than that in pair 2, despite the shorter distance between V(III) ions (7.5 Å in pair 1 *vs.* 8.65 Å in pair 2, Fig. S19, ESI†). Superexchange calculations for more distant pairs in **3** (V···V = >10 Å, Fig. S18, ESI†) yield even smaller exchange parameters (<10^{-4} cm^{-1}). These results provide evidence that the dimer-like spin coupling model is indeed good theoretical platform for the description of magnetic properties and HF/EPR spectra of compound **3**, albeit formally vanadium chains (Fig. S18, ESI†) can also be regarded as strongly alternating spin chains due to the presence of a weak magnetic coupling between dimers (J = –0.09 cm^{-1}, Fig. S20, ESI†) Therefore, our superexchange calculations explain in a natural way the origin of the dimer-like character of the spin coupling between V(III) ions in **3**, as they indicate that the spin coupling in pair 2 (with V···V = 8.65 Å, Fig. 4b and Fig. S19b, ESI†) through the π-stacking strongly dominates over the spin coupling in other vanadium pairs in compound **3**.

In this respect, it is also important to note that there is direct experimental evidence of the efficiency of exchange interactions between 3d-magnetic ions conducted by the π-stacking of planar macrocyclic ligands, as exemplified by cobalt compounds composed of isolated Co(II) complexes[31] in which rather strong ferromagnetic spin coupling ($J \approx 2$ cm^{-1}) between Co^{2+} ions is mediated through the π-stacking contacts of the pyridine rings of the dpamH ligands.

AC susceptibility measurements on the complexes revealed no SMM behavior, both with and without an applied magnetic field.

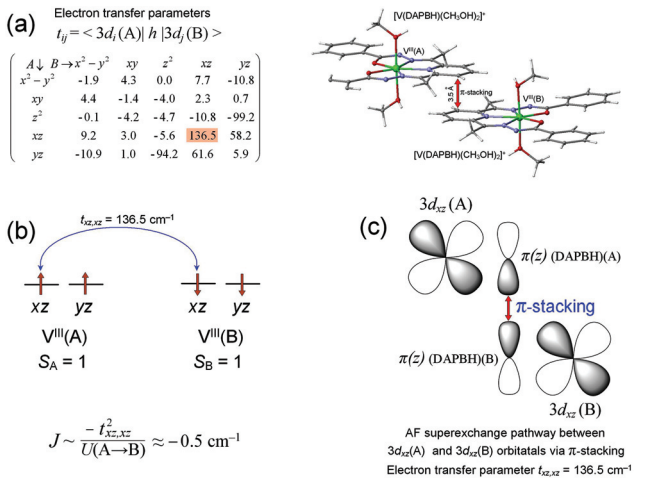

Fig. 10 On the origin of AF spin coupling in **3**. (a) Calculated electron transfer parameters $t_{ij} = \langle 3d_i(\mathrm{A})|h|3d_j(\mathrm{B})\rangle$ (in cm^{-1}) connecting magnetic orbitals of the V^{III}(A) and V^{III}(B) centers in pair 2 (see the ESI† for computational details). The largest matrix element $t_{xz,xz}$ = 136.5 cm^{-1} is diagonal (marked in orange), (b) $t_{xz,xz}$ connects two half-filled magnetic orbitals 3d$_{xz}$(A) and 3d$_{xz}$(B) resulting in AF spin coupling with $J \sim -(t_{xz,xz})^2/U(\mathrm{A} \rightarrow \mathrm{B}) \approx -0.5$ cm^{-1} (where U(A → B) is the charge-transfer energy, ~40 000 cm^{-1} (5 eV)), (c) the orbital scheme of the superexchange pathway: in each of the two $[V(DAPBH)(CH_3OH)_2]^+$ complexes (A,B), magnetic 3d$_{xz}$ orbital overlaps with the collective π(*z*)(DAPBH) molecular orbital of the planar DAPBH ligand; these orbitals interact *via* the π-stacking contact of two DAPBH ligands resulting in an efficient superexchange pathway with $t_{xz,xz}$ = 136.5 cm^{-1} and $J \approx -0.5$ cm^{-1}.

Conclusions

In summary, three mononuclear pentagonal-bipyramidal complexes of V(III) with the equatorial pentadentate N_3O_2 ligand (2,6-diacethylpyridinebis(benzoic acid hydrazone), H_2DAPBH) were synthesized and characterized structurally and magneti-

cally, $[V(H_2DAPBH)Cl_2]Cl{\cdot}C_2H_5OH$ (**1**), $[V(HDAPBH)(NCS)_2]{\cdot}0.5CH_3CN{\cdot}0.5CH_3OH$ (**2**) and $[V(DAPBH)(CH_3OH)_2]Cl{\cdot}CH_3OH$ (**3**). They show paramagnetic behavior arising from two unpaired electrons ($S = 1$) with a positive axial anisotropy ZFS parameter ($D \approx +4$ cm^{-1}, $E \approx 0$) and pronounced dimer-like antiferromagnetic spin coupling between two neighboring vanadium centers ($J = -1.1$ cm^{-1}), as has been established for compound **3** from high-frequency/high-field EPR and low-temperature magnetization measurements. Detailed superexchange calculations for compound **3** provide evidence that the long-range spin coupling between distant V(III) ions (8.65 Å) is mediated through π-stacking contacts between the planar DAPBH ligands of two neighboring $[V(DAPBH)(CH_3OH)_2]^+$ complexes; the absence of π-stacking in other vanadium pairs results in much smaller exchange parameters that account for the dimer-like character of the spin coupling in **3**. Complexes **1–3** are the first representatives of vanadium PBP complexes with planar pentadentate Schiff-base ligands in the equatorial plane.

Conflicts of interest

There are no conflicts to declare.

Acknowledgements

This work was supported by the Russian Science Foundation (project no. 18-13-00264). Structural research was performed within the state assignment for the ISSP RAS. R. K. acknowledges support by BMBF *via* project SPINFUN no. 13XP5088 (the Section "HF-EPR study", Interpretation). L. S. acknowledges support from Landesgraduiertenförderung Baden-Württemberg (the Section "HF-EPR study", HF-EPR and Low-T SQUID experiments, data analysis, DFT calculations) and C. K. acknowledges support by Deutsche Forschungsgemeinschaft through project KO5480/1-1 (the Section "HF-EPR study", data analysis, discussion). O. V. M. and A. N. V. acknowledge support by the Ministry of Education and Science of the Russian Federation in the framework of Increase Competitiveness Program of NUST "MISiS" Grant No. K2-2020-008; by Act 211 of the Government of Russian Federation, Contracts No. 02.A03.21.0004 and No. 02.A03.21.0011 (the Section "DC Magnetic Susceptibility Studies").

References

1 (*a*) A. K. Bar, N. Gogoi, C. Pichon, V. M. Goli, M. Thlijeni, C. Duhayon, N. Suaud, N. Guihery, A. L. Barra, S. Ramasesha and J.-P. Sutter, *Chem. – Eur. J.*, 2017, **23**, 4380; (*b*) A. K. Bar, P. Kalita, J.-P. Sutter and V. Chandrasekhar, *Inorg. Chem.*, 2018, **57**, 2398; (*c*) V. D. Sasnovskaya, V. A. Kopotkov, A. V. Kazakova, A. D. Talantsev, R. B. Morgunov, S. V. Simonov, L. V. Zorina, V. S. Mironov and E. B. Yagubskii, *New J. Chem.*, 2018, **42**, 14883; (*d*) A. K. Mondal, A. Mondal, B. Dey and S. Konar, *Inorg. Chem.*, 2018, **57**, 9999; (*e*) V. A. Kopotkov, D. V. Korchagin, V. D. Sasnovskaya, I. F. Gilmutdinov and E. B. Yagubskii, *Magnetochemistry*, 2019, **5**, 58.

2 (*a*) N. Gogoi, M. Thlijeni, C. Duhayon and J.-P. Sutter, *Inorg. Chem.*, 2013, **52**, 2283; (*b*) V. D. Sasnovskaya, V. A. Kopotkov, A. D. Talantsev, R. B. Morgunov, E. B. Yagubskii, S. V. Simonov, L. V. Zorina and V. S. Mironov, *Inorg. Chem.*, 2017, **56**, 8926; (*c*) C. Pichon, N. Suaud, C. Duhayon, N. Guihery and J.-P. Sutter, *J. Am. Chem. Soc.*, 2018, **140**, 7698; (*d*) L. V. Zorina, S. V. Simonov, V. D. Sasnovskaya, A. D. Talantsev, R. B. Morgunov, V. S. Mironov and E. B. Yagubskii, *Chem. – Eur. J.*, 2019, **25**, 14583.

3 (*a*) I. Ivanovic-Burmazovic and K. Andjelkovic, *Adv. Inorg. Chem.*, 2004, **55**, 315 and references therein. (*b*) C. Pichon, B. Elrez, V. Bereau, C. Duhayon and J.-P. Sutter, *Eur. J. Inorg. Chem.*, 2018, 340; (*c*) M. Gerloch, I. Morgenstern-Badarau and J.-P. Audiere, *Inorg. Chem.*, 1979, **18**, 3220; (*d*) M. Gerloch and I. Morgenstern-Badarau, *Inorg. Chem.*, 1979, **18**, 3225; (*e*) M. Gerloch and R. L. Hanton, *Inorg. Chim. Acta*, 1981, **49**, 37.

4 (*a*) E. L. Gavey and M. Pilkington, *Chem. Rev.*, 2015, **296**, 125; (*b*) A. K. Bar, C. Pichon and J.-P. Sutter, *Coord. Chem. Rev.*, 2016, **308**, 346.

5 (*a*) O. Waldmann, *Inorg. Chem.*, 2007, **46**, 10035; (*b*) F. Neese and D. A. Pantazis, *Faraday Discuss.*, 2011, **148**, 229.

6 (*a*) V. S. Mironov, L. F. Chibotaru and A. Ceulemans, *J. Am. Chem. Soc.*, 2003, **125**, 9750; (*b*) X.-Y. Wang, C. Avendaño and K. R. Dunbar, *Chem. Soc. Rev.*, 2011, **40**, 3213 and references therein (*c*) R. A. Layfield and M. Murugesu, *Lanthanides and Actinides in Molecular Magnetism*, Wiley-VCH, 2015.

7 (*a*) Y.-Z. Zhang, B.-W. Wang, O. Sato and S. Gao, *Chem. Commun.*, 2010, **46**, 6959; (*b*) Y.-C. Chen, J.-L. Liu, L. Ungur, J. Liu, Q.-W. Li, L.-F. Wang, Z.-P. Ni, L. F. Chibotaru, X.-M. Chen and M.-L. Tong, *J. Am. Chem. Soc.*, 2016, **138**, 2829; (*c*) R. Ruamps, L. J. Batchelor, R. Guillot, G. Zakhia, A. L. Barra, W. Wernsdorfer, N. Guihéry and T. Mallah, *Chem. Sci.*, 2014, **5**, 3418; (*d*) R. Ruamps, L. J. Batchelor, R. Maurice, N. Gogoi, P. Jiménez-Lozano, N. Guihéry, C. de Graaf, A. L. Barra, J.-P. Sutter and T. Mallah, *Chem. – Eur. J.*, 2013, **19**, 950; (*e*) R. Ruamps, R. Maurice, L. J. Batchelor, M. Boggio-Pasqua, R. Guillot, A. L. Barra, J. Liu, E.-E. Bendeif, S. Pillet, S. Hill, T. Mallah and N. Guihéry, *J. Am. Chem. Soc.*, 2013, **135**, 3017.

8 (*a*) Y.-F. Deng, B. Yao, P.-Z. Zhan, D. Gan, Y.-Z. Zhang and K. R. Dunbar, *Dalton Trans.*, 2019, **48**, 3243; (*b*) Y. V. Manakin, V. S. Mironov, T. A. Bazhenova, K. A. Lyssenko, I. F. Gilmutdinov, K. S. Bikbaev, A. A. Masitov and E. B. Yagubskii, *Chem. Commun.*, 2018, **54**, 10084; (*c*) F. J. Birk, D. Pinkowicz and K. R. Dunbar, *Angew. Chem., Int. Ed.*, 2016, **55**, 11368; (*d*) J. Liu, Y.-C. Chen, J.-L. Liu, V. Vieru, L. Ungur, J.-H. Jia, L. F. Chibotaru, Y. Lan, W. Wernsdorfer, S. Gao, X.-M. Chen and M.-L. Tong, *J. Am. Chem. Soc.*, 2016, **138**, 5441;

(*e*) Y.-S. Ding, N. F. Chilton, R. E. Winpenny and Y.-Z. Zheng, *Angew. Chem., Int. Ed.*, 2016, **55**, 16071; (*f*) S. K. Gupta, T. Rajeshkumar, G. Rajaraman and R. Murugavel, *Chem. Sci.*, 2016, **7**, 5181.

9 (*a*) D. E. Freedman, D. M. Jenkins and J. R. Long, *Chem. Commun.*, 2009, 4829; (*b*) K. C. M. Westrup, M.-E. Boulon, P. Totaro, G. G. Nunes, D. F. Back, A. Barison, M. Jackson, C. Paulsen, D. Gatteschi, L. Sorace, A. Cornia, J. F. Soares and R. Sessoli, *Chem. – Eur. J.*, 2014, **20**, 13681.

10 (*a*) S. Ferlay, T. Mallah, R. Ouhes, P. Veillet and M. Verdaguer, *Nature*, 1995, **378**, 701; (*b*) Ø. Hatlevik, W. E. Buschmann, J. Zhang, J. L. Manson and J. S. Miller, *Adv. Mater.*, 1999, **11**, 914; (*c*) S. M. Holmes and G. S. Girolami, *J. Am. Chem. Soc.*, 1999, **121**, 5593.

11 J. Krzystek, A. T. Fiedler, J. J. Sokol, A. Ozarowski, S. A. Zvyagin, T. C. Brunold, J. R. Long and J. Telser, *Inorg. Chem.*, 2004, **43**, 5645.

12 T. J. Giordano, G. J. Palenik, R. C. Palenik and D. A. Sullivan, *Inorg. Chem.*, 1979, **18**, 2445.

13 CrysAlisPro Software System, *Rigaku Oxford Diffraction, version 1.171.39*, Rigaku, Tokyo, Japan, 2018.

14 G. M. Sheldrick, *Acta Crystallogr., Sect. A: Found. Crystallogr.*, 2008, **64**, 112.

15 P. Comba, M. Großhauser, R. Klingeler, C. Koo, Y. Lan, D. Müller, J. Park, A. Powell, M. J. Riley and H. Wadepohl, *Inorg. Chem.*, 2015, **54**, 11247.

16 S. Stoll and A. Schweiger, *J. Magn. Reson.*, 2006, **178**, 42.

17 F. Neese, *Chem. Phys. Lett.*, 2000, **325**, 93.

18 A. Schäfer, C. Huber and R. Ahlrichs, *J. Chem. Phys.*, 1994, **100**, 5829.

19 F. Neese, *Wiley Interdiscip. Rev.: Comput. Mol. Sci.*, 2012, **2**, 73.

20 F. Neese and E. I. Solomon, *Inorg. Chem.*, 1998, **37**, 6568.

21 (*a*) C. E. Schaeffer and C. K. Jorgensen, *Mol. Phys.*, 1965, **9**, 401; (*b*) C. E. Schaffer, *Struct. Bonding*, 1968, **5**, 68.

22 (*a*) V. S. Mironov, L. F. Chibotaru and A. Ceulemans, *Phys. Rev. B: Condens. Matter Mater. Phys.*, 2003, **67**, 014424; (*b*) E. N. Zorina, N. V. Zauzolkova, A. A. Sidorov, G. G. Aleksandrov, A. S. Lermontov, M. A. Kiskin, A. S. Bogomyakov, V. S. Mironov, V. M. Novotortsev and I. L. Eremenko, *Inorg. Chim. Acta*, 2013, **396**, 108; (*c*) V. S. Mironov, *Inorg. Chem.*, 2015, **54**, 11339; (*d*) V. D. Sasnovskaya, V. A. Kopotkov, A. D. Talantsev, R. B. Morgunov, E. B. Yagubskii, S. V. Simonov, L. V. Zorina and V. S. Mironov, *Inorg. Chem.*, 2017, **56**, 8926.

23 (*a*) M. Llunell, D. Casanova, J. Cirera, P. Alemany and S. Alvarez, *SHAPE (V. 2.1)*, Barcelona, 2013; (*b*) S. Alvarez, P. Alemany, D. Casanova, J. Cirera, M. Llunell and D. Avnir, *Coord. Chem. Rev.*, 2005, **249**, 1693.

24 J. Krzystek, S. A. Zvyagin, A. Ozarowski, S. Trofimenko and J. Telser, *J. Magn. Reson.*, 2006, **178**, 174.

25 E. Ferentinos, C. P. Raptopoulou, V. Psycharis, A. Terzis, J. Krzystek and P. Kyritsis, *Polyhedron*, 2018, **151**, 177.

26 S. Tripathi, S. Vaidya, K. U. Ansari, N. Ahmed, E. Rivière, L. Spillecke, C. Koo, R. Klingeler, T. Mallah, G. Rajaraman and M. Shanmugam, *Inorg. Chem.*, 2019, **58**, 9085.

27 S. Blundell, *Magnetism in Condensed Matter*, Oxford Univ. Press, Oxford, 2014.

28 K. A. Campbell, E. Yikilmaz, C. V. Grant, W. Gregor, A.-F. Miller and R. D. Britt, *J. Am. Chem. Soc.*, 1999, **121**, 4714.

29 T. Matsukawa, H. Mino, D. Yoneda and A. Kawamori, *Biochemistry*, 1999, **38**, 4072.

30 C. Mennerich, H.-H. Klauss, M. Broekelmann, F. J. Litterst, C. Golze, R. Klingeler, V. Kataev, B. Buechner, S.-N. Grossjohann, W. Brenig, M. Goiran, H. Rakoto, J.-M. Broto, O. Kataeva and D. J. Price, *Phys. Rev. B: Condens. Matter Mater. Phys.*, 2006, **73**, 174415.

31 V. Tangoulis, M. Lalia-Kantouri, M. Gdaniec, C. Papadopoulos, V. Miletic and A. Czapik, *Inorg. Chem.*, 2013, **52**, 6559.